erwise the maximum slopes at the entries V_{in} and V_{in} must be limited such that the node potential V_{N1} can follow at the same speed.

Discussion: A prototype optimised for low area consumption and high latch-up security fitted in an area $244 \times 450 \mu m^2$. The parameters A and B were chosen to be $A = 1.5$, $B = 2$, which leads to $I_r = 3I_c$. The MOS transistor's thin-oxide gate dimensions for $I_c = 9\mu A$ measured in (W/μm)/(L/μm) were selected to be for M1, M2, M4, M6: 15/10, M3, M5: 15/4, M7: 10/4, M8: 10/10, M9, M10: 10/5. D1 was made by a p-MOS drain-substrate diode.

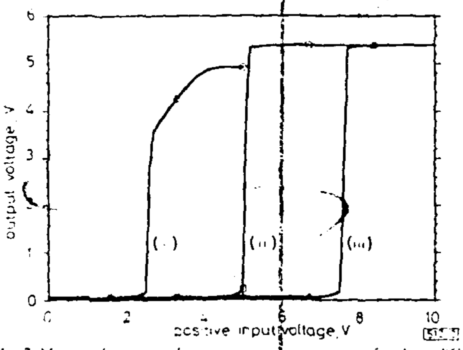

Fig. 2 *Measured output voltage at zero output current for three different boundary conditions*

V_{out} measured at $V_{DD} = 5V$, $I_{out} = 0$, $V_{in}^{-} = 0 ... V_H$ in steps of 0.1V, and
(i) $V_{in}^{-} = 2.5V$, $V_H = 5V$
(ii) $V_{in}^{-} = 5.0V$, $V_H = 35V$
(iii) $V_{in}^{-} = 7.5V$, $V_H = 70V$

Fig. 2 shows measurements of V_{out} against V_{in}^{+} for three different boundary conditions. Curve (iii) was obtained at high-voltage conditions with $V_{in}^{-} = 7.5V$ and $V_H = 70V$. The unloaded output jumps at $V_{in}^{+} = V_{in}^{-}$ from a near-zero value to its maximum limited by D3 to 5.4V. Curve (i) was measured under low voltage conditions, i.e. $V_H = V_{DD} = 5V$ and $V_{in}^{+}, V_{in}^{-} \le V_{DD}$. Two additional effects are observed:

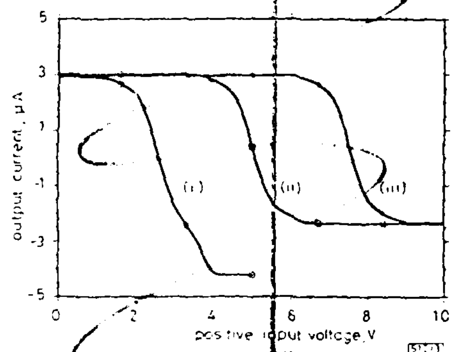

Fig. 3 *Measured output current at $V_{in}^{-} = 2.5V$ for three different boundary conditions*

I_{out} measured at $V_{out} = 2.5V$, otherwise same measurement setup as in Fig. 2

(i) The maximum output voltage is reduced to 4.9V, the last 100mV are dropped over the desaturated current source I_r.

(ii) The output voltage jumps as expected at $V_{in}^{+} = V_{in}^{-} = 2.5V$, but not to its maximum.

If both V_{in}^{+} and V_{in}^{-} are less then V_{th}, the potential of node N1 (V_{N1}) may be less than V_{DD} also, and we have $V_{out} \le V_{N1}$. For $V_{in}^{-} = V_{DD}$ the full output voltage swing of 0–V_{DD} is available at the output, as demonstrated by curve (ii).

Fig. 3 shows output currents measured with a constant $V_{out} = 2.5V$, otherwise the setup is the same as explained above. The maximum transconductance is $\Delta I_{out}/\Delta V_{in}^{+} = 5\mu A/V$ and I_{out} varies between −2.4 and 3.0μA. An exception of $I_{out,min} = -4.2\mu A$ is seen at $V_H = 5V$, which may be due to desaturation of the current source I_r.

Acknowledgments: The author would like to thank E. Vittoz, F. Krummenacher and M. Declercq for invaluable discussions and advice and specifically M. Declercq for encouraging and supporting the project.

21 December 1993
Electronics Letters Online No: 19940235

M. Schubert (*Swiss Federal Institute of Technology (EPFL), Electronics Laboratories, EL-LEG Ecublens, CH-1015 Lausanne, Switzerland*)

References

1 BALIGA, B.J.: 'An overview of smart power technology', *IEEE Trans.*, July 1991, ED-38, (7), pp. 1568–1575
2 PARPIA, Z., SALAMA, C.A.T., and HADAWAY, R.A.: 'Modeling and characterization of CMOS-compatible high-voltage device structures', *IEEE Trans.*, November 1989, ED-34, (11), pp. 2335–2343
3 APEL, U., HABERKOTTE, E., and HOFFLINGER, B.: 'High-voltage CMOS transistors in a low-voltage CMOS process'. Proc. Int. Symp. on Signals, Systems and Electronics, 1989, University of Erlangen, pp. 52–55, URSI
4 DECLERCQ, M., CLEMENT, F., SCHUBERT, M., HARB, A., and DUTOIT, M.: 'Design and optimization of high-voltage CMOS devices compatible with a standard 5V CMOS technology'. Proc. IEEE 1993 Custom Integrated Circuits Conf., 1993, Paper 24.6
5 DECLERQ, M., SCHUBERT, M., and CLEMENT, F.: '5V-to-75V CMOS output interface circuits'. Proc. 40th Int. Solid-State Circuits Conf., 1993, Paper TP 10.6

Induced second-harmonic generation in planar waveguides by an externally applied periodic DC electric field: Efficiency as a function of field structure

M.L. Brauer, I. Dajani and J.J. Kester

Indexing terms: Optical harmonic generation, Optical waveguide theory, Finite element analysis

The efficiency of second-harmonic generation (SHG) induced by an externally applied periodic DC electric field was investigated. A finite element method was used to find the static electric field due to different interdigitated electrode structures. The resulting fields were used to calculate the overlap integrals which determine the SHG efficiency in an optical waveguide. The results show that there are reasonable differences in SHG efficiencies for the structures investigated.

Efficient frequency doubling of radiation has been observed in germanium doped silica fibres [1] and planar waveguides [2]. All of the theories that have been proposed to explain this phenomenon are based on the hypothesis that an internal periodic DC electric field is responsible for a nonvanishing second-order susceptibility, $\chi^{(2)}$ and the necessary quasiphase matching for efficient SHG [3]. This $\chi^{(2)}$ is found to be proportional to the product of the third-order susceptiblity, $\chi^{(3)}$, and this induced field. The periodic DC electric field induced in silica can be generated by several methods, such as seeding by the second harmonic [3] and by applying an external periodic DC electric field [4]. Traditionally, the external periodic DC electric fields have been generated using interdigitated electrode structures. However, little has been done to understand the effect of using different electrode structures on the efficiency of SHG.

We investigated the efficiency of SHG in an optical, thin-film, planar waveguide as a function of the externally applied periodic DC electric field. Three DC fields were simulated using interdigitated electrode structures with varying electrode widths and spacings. These externally applied periodic DC electric fields induce the internal polarisation responsible for efficient SHG.

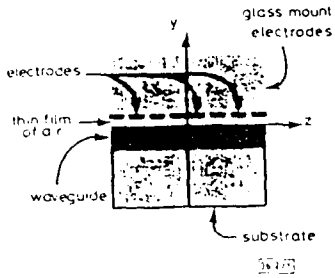

Fig. 1 *Cross-section of waveguide structure including interdigitated electrodes*

The simulated structures consisted of a thin-film waveguide deposited on a silica substrate with the interdigitated electrodes mounted on glass and situated on a thin film of air above the waveguide as shown in Fig. 1. For all three structures investigated, the thickness of the thin film of air was 0.5μm and the thickness of the waveguide was 2μm. The indices of refraction of the waveguide and substrate at the fundamental wavelength (1064 nm) are 1.532 and 1.4496, respectively. For the second harmonic, the corresponding indices are 1.471 and 1.4607. We analysed the SHG using a TM_0 mode for both the fundamental and the second harmonic. The periodicity for quasiphase matching was determined from the expression

$$\Delta z = \left| \frac{2\pi}{2\beta_\omega - \beta_{2\omega}} \right| \qquad (1)$$

where β_ω is the propagation constant for the fundamental and $\beta_{2\omega}$ is the propagation constant for the second harmonic. For the three structures analysed, the electrode width was varied (2.5, 5.0, and 7.5μm) while the periodicity (20μm) was kept constant.

To compare the relative efficiencies of the different electrode structures, a finite element method computer simulation was used to find the static electric field due to the electrodes in the waveguide. The results were then used to calculate the growth of the second harmonic along the direction of propagation, z, in the planar waveguide. The expression for this growth was derived by applying the normal mode analysis to the wave equation and using the slowly-varying envelope approximation in a manner similar to standard second-harmonic efficiency derivations [5]. The rate of growth of the complex amplitude of the second harmonic, $a_{2\omega}$, is found to be proportional to the overlap integral and is given by

$$\frac{da_{2\omega}}{dz} \propto \chi^{(2)} e^{-i\Delta\beta z} \int E_{dc}(y) E_\omega(y) E^*_{2\omega}(y)\, dy \qquad (2)$$

where E_{dc} is the x component of the externally applied periodic DC field due to the electrodes, E_ω and $E_{2\omega}$ represent the transverse mode distribution of the fundamental and second harmonic, respectively, and $\Delta\beta$ is the phase mismatch given by $\Delta\beta = \beta_{2\omega} - 2\beta_\omega$. Note that we have assumed that the amplitude for the fundamental is much larger than that for the second harmonic. The power of the second harmonic is then given by the square of the modulus of the integral of eqn. 2 along z and is expressed as

$$P(2\omega) \propto \left| \chi^{(2)} \iint E_{dc}(y) E_\omega(y) E^*_{2\omega}(y) e^{-i\Delta\beta z}\, dy dz \right|^2 \qquad (3)$$

This equation was used to compute the second-harmonic power for the three different electrode structures.

The profiles of the x-component of the static electric field, E_{dc}, for the three different electrode structures are shown in Fig. 2. The plots are shown from the centre of the spacing between the electrodes to the centre of the electrodes for different depths ($y = 0$, -1μm, and -2μm) in the waveguide and is symmetric across the entire structure. The accuracy of the computer code was checked by simulating cases with geometries that have known analytical solutions, and the error was found to be less than 1%.

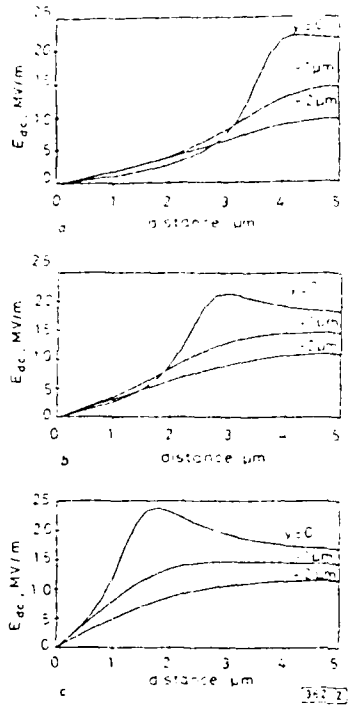

Fig. 2 *x-component of E_{dc} for three different electrode structures*

a Electrode width = 2.5μm
b Electrode width = 5.0μm
c Electrode width = 7.5μm

We compared the power generated in the second harmonic for the three different structures normalised to the structure with the lowest efficiency. The results are summarised in Table 1.

Table 1: Comparison of power generated in second harmonic for three structures

Electrode width [μm]	2.5	5.0	7.5
Normalised SHG power	1.0	1.75	2.30

We conclude that there is over a factor of 2 difference in the efficiency of SHG based on the relative width of the electrode compared to the periodicity of the electrode structure. The difference indicates that structures with wider electrodes (while not exceeding the dielectric breakdown between the electrodes) have more efficient SHG.

Acknowledgments: M. L. Brauer would like to acknowledge the Department of Electrical Engineering at the U.S. Air Force Academy for allowing her sabbatical leave to do this work. This work was performed while I. Dajani held a National Research Council-FJSRL Research Associateship.

6 December 1993
Electronics Letters Online No. 19940193

M. L. Brauer, I. Dajani and J. J. Kester (*Frank J. Seiler Research Laboratory, US Air Force Academy, CO 80840-6272, USA*)

References

1 ÖSTERBERG, U., and MARGULIS, W.: 'Dye laser pumped by Nd YAG laser pulses frequency doubled in an optical fiber', *Opt. Lett.*, 1986, 11, pp. 516–518

2 KESTER, J.J., WOLF, P.J., and WHITE, W.R.: 'Second-harmonic generation in planar waveguides of doped silica', *Opt. Lett.*, 1992, 17, pp. 1779–1781

3 STOLEN, R.H., and TOM, H.W.K.: 'Self-organized phase-matched harmonic generation in optical fibers', *Opt. Lett.*, 1987, 12, pp. 585–587

4 WEITZMAN, P.S., KESTER, J.J., and ÖSTERBERG, U.: 'Electric field induced second harmonic generation in germanium doped silica planar waveguides', submitted to *Opt. Lett.*

5 SHEN, Y.R.: 'The principles of nonlinear optics' (Wiley-Interscience, New York, 1984)

New wideband, 0.67λ_g circumference 180° hybrid ring coupler

M.-H. Murgulescu, E. Moisan, P. Legaud, E. Penard and I. Zaquine

Indexing terms: MMICs, Transmission lines, Waveguide couplers

A new 180° hybrid ring coupler is reported. This coupler uses coplanar waveguides and has a very small circumference of only 0.67λ_g. A bandwidth greater than one octave is demonstrated.

Introduction: Miniaturised 180° hybrid couplers are required for monolithic integration. Some attempts have already been made to reduce the size of the well known 1.5λ_g circumference microstrip rat-race coupler [1–4], but this has led to narrowband operation. We previously proposed [5] the use of uniplanar waveguides to achieve both small size and wideband operation, but our structure had the E-port fed in a slotline, which is the major drawback when full coplanar access is required. In this Letter we propose a new wideband, small-size coupler having all the ports fed coplanar. No space costly transitions are used.

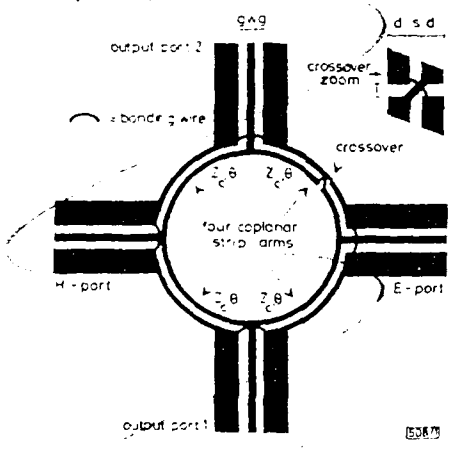

Fig. 1 *Hybrid ring coupler*

Coupler design: The coupler is shown in Fig. 1. It has a ring topology, consisting of four arms. Each arm is made of a transmission line. In a symmetrical design all the four coupler arms are identical. In such a case there is one degree of freedom (the arm electrical length θ). The design equation is

$$Z_c = Z_0\sqrt{2}\sqrt{1-\cos^2\theta} \qquad (1)$$

where Z_0 is the port impedance (usually 50Ω) and θ is the electrical length of one arm at the central frequency f_0. From eqn. 1 it is obvious that the minimum circumference of the coupler is 0.5λ_g. Simulations indicate that wideband operation is obtained for a relatively small value of θ. Our design has been made with $\theta = 60°$ leading to a characteristic impedance Z_c of 57.6Ω. Symmetric coplanar strips are used as transmission lines because they allow an easy crossover of the two strips. Because $s \ll d$ (Fig. 1) we computed the propagation characteristics of the coplanar strip line as for a slotline, using the Cohn method [6]. The crossover is necessary to provide the 180° phase shift needed at the E-port. The crossover may be placed at any position in its arm. 150μm diameter bonding wires have been used to realise the crossover and to eliminate the even propagation mode on the access coplanar lines. Their length should be kept as short as possible to minimise wire self-inductance. For this reason is important to minimise both coplanar line total width $w+2g$ and the crossover dimensions. However, an extreme crossover size reduction (at the photolithographic limit) leads to undesired coupling by the gap capacitance. Power is radiated at the coplanar strip apertures created by the crossover, but a mutual radiated field cancellation effect is present because the electric fields in the two apertures have opposite signs. Coplanar access lines are connected to the coplanar strips using a tee junction. No attempt has been made to model this junction because the dimensions of both the access lines (w and g) and the coplanar strips gap (s) are very small.

An important feature of the coupler is that the output magnitude and the phase balances are excellent, as the crossover provides an almost perfect 180° phase shift in the whole frequency range. This is an advantage with respect to the microstrip implementations of the 180° hybrid, where the $\lambda_g/2$ delay line gives a 180° phase shift only at the centre frequency.

The coupler has been fabricated on an alumina substrate (ε_r = 9.9, h = 254μm, metal thickness 4μm) without a ground plane. The coupler centre frequency is f_0 = 6GHz. The most relevant geometrical parameters are listed in Table 1.

Table 1: Coupler geometrical parameters

θ	Z	Circumference	Ring radius	Coplanar strip width d	Coplanar strip gap s	Crossover coplanar strip gap t	50Ω access coplanar line dimensions
deg	Ω		μm	μm	μm	μm	μm
60.0	57.6	0.67λ_g	3478	300	60	100	w = 50, g = 30

We point out that the coupler topology described here is also suitable for an asymmetric design (i.e. when adjacent arms are not identical). The coupler can be transformed into a balun by simply closing the H-port on a 50Ω impedance.

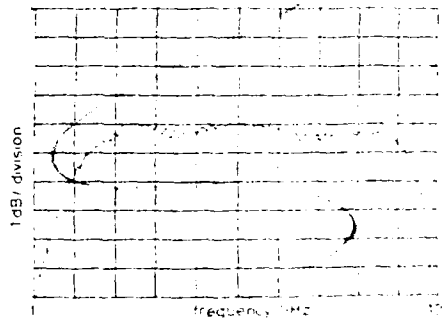

Fig. 2 *Coupler transmission when fed to H-port (magS$_{21}$, H)*

Experimental results: The coupler has been tested between 1 and 10GHz. The effect of connectors and access coplanar lines are included. The latter are relatively long (7mm input ports and 4.5mm output ports access lines lengths) degrading the transmission. Therefore the intrinsic coupler transmission is ≈0.5dB better than measured. For the same reason intrinsic reflection loss is somewhat better, too. Coupler transmission and reflection loss are shown in Figs. 2 and 3. The coupler measured characteristics in